Chinese Chemical Letters 37 (2026) 112057

Contents lists available at ScienceDirect

Chinese Chemical Letters

journal homepage: www.elsevier.com/locate/cclet

Durable anode-free lithium metal batteries enabled by a lithiophilic Cu-Zn Solid-Solution with accelerated interfacial Li^+ diffusion kinetics

Fan Zhang[a,1], Zizhu Guo[a,1], Jin Wang[a], Dan Sun[a], Xiaobing Huang[b,*], Qi Zhang[a], Yougen Tang[a], Yusi Yang[a,*], Haiyan Wang[a,*]

[a] Hunan Provincial Key Laboratory of Chemical Power Sources, College of Chemistry and Chemical Engineering, Central South University, Changsha 410083, China

[b] College of Chemistry and Chemical Engineering, Hunan University of Arts and Science, Changde 415000, China

ARTICLE INFO

Article history:
Received 24 September 2025
Revised 29 October 2025
Accepted 3 November 2025
Available online 6 November 2025

Keywords:
Anode-free lithium metal batteries
Solid solution
Interfacial stability
Lithiophilicity
High energy density batteries

ABSTRACT

Cu-Zn solid solutions are investigated as advanced current collector materials for anode-free Li metal batteries (AFLMBs), addressing the limited lithiophilicity and slow Li^+ diffusion kinetics inherent to conventional Cu foil. Benefiting from the uniform distribution of lithiophilic Zn, Cu-Zn solid solutions demonstrated enhanced lithiophilicity and accelerated Li^+ diffusion, which effectively facilitated uniform and reversible lithium deposition. First-principles calculations confirmed that Cu-Zn solid solutions, particularly $Cu_{62}Zn_{38}$, exhibited stronger Li adsorption and reduced diffusion barriers compared to Cu. Unlike alloy-prone metal coatings (*e.g.*, Cu@Zn and thermally processed Cu@Zn) that sacrifice interfacial stability for lithiophilicity, Cu-Zn solid solution maintains robust electrode-electrolyte interfaces due to its alloying inertness. *Ex-situ* SEM and COMSOL simulations revealed dendrite-suppressed and homogeneous Li deposition on $Cu_{62}Zn_{38}$. In anode-free full cells, $Cu_{62}Zn_{38}$ achieves a capacity retention of 55.1 % after 150 cycles, far exceeding Cu foil (13.8 %). This work establishes Cu-Zn solid solutions current collectors as a scalable solution for high-energy-density AFLMBs.

© 2026 Published by Elsevier B.V. on behalf of Chinese Chemical Society and Institute of Materia Medica, Chinese Academy of Medical Sciences.

Rising global energy demands and environmental concerns require advanced energy storage technologies with high energy density and long cycle life [1,2]. While conventional lithium-ion batteries (LIBs) dominate commercially, they are approaching theoretical performance limits, driving the development of next-generation alternatives [3,4]. Lithium metal batteries (LMBs) represent promising candidates for the next-generation of high energy batteries due to ultrahigh theoretical specific capacity (3860 mAh/g) and low working electrochemical potential (−3.04 V) of lithium anode [5,6]. Anode-free lithium metal batteries (AFLMBs) further enhance energy density by eliminating excessive Li metal [7,8], simplifying manufacturing process while avoiding lithium anode issues. However, AFLMBs inherit intrinsic challenges of LMBs, including dendritic growth, unstable solid-electrolyte interphase (SEI), and parasitic reactions, while facing added complexity from absent lithium reservoirs [9,10]. Crucially, lacking pre-existing lithium metal induces nonuniform deposition and irreversible lithium loss, accelerating dendrite formation and capacity degradation [11].

Significant advances in electrolyte design [12–15], interface engineering [16–18], and current collector design [19–21] provide promising strategies to overcome challenges and unlock the potential of AFLMBs for next-generation energy storage applications. As we know, the current collector plays a crucial role in regulating lithium nucleation behaviors and deposition morphologies, with surface lithiophilicity and Li^+ diffusion kinetics being the key factors. Conventional copper (Cu) foil has relatively low lithiophilicity, leading to inhomogeneous lithium deposition and dendrite formation [22]. Surface coating techniques (*e.g.*, carbon, metal or metal oxide coatings) have been employed to improve interface lithiophilicity and promote uniform lithium deposition, further bringing AFLMBs closer to practical deployment [23–25].

Metals that alloy with lithium (Zn, Sn, Ag, Au, *etc.*) have been extensively studied as surface coatings due to their strong lithiophilicity, which could promote uniform lithium nucleation and suppresses dendrite formation [26–28]. However, the alloying process inevitably involves substantial volume expansion, leading to interface degradation and poor cycling reversibility. To mitigate these effects, recent efforts have focused on constructing inter-

* Corresponding authors.
E-mail addresses: hxb220170@126.com (X. Huang), nameyys@163.com (Y. Yang), wanghy419@csu.edu.cn (H. Wang).
[1] These authors contributed equally to this work.

https://doi.org/10.1016/j.cclet.2025.112057
1001-8417/© 2026 Published by Elsevier B.V. on behalf of Chinese Chemical Society and Institute of Materia Medica, Chinese Academy of Medical Sciences.

metallic alloy coatings to buffer volume effects, but such strategies remain limited by inherent alloying-induced fluctuations, and also increase fabrication complexity and costs. Accordingly, we turned our attention to solid-solution alloy foils, which offer a promising yet unexplored approach for AFLMBs. Specifically, Cu-Zn solid-solution (brass) have emerged as a promising candidate due to the high lattice compatibility between Cu and Zn, which enables the formation of solid-solution phases with uniformly distributed Zn atoms within stable Cu lattice. These embedded Zn sites not only act as effective lithiophilic centers, but also inert to lithium alloying reaction due to the refrain of Cu matrix, ensuring both interfacial lithiophilicity and stability during cycling. Furthermore, brass foil is low-cost, scalable, and compatible with conventional foil manufacturing, making it an attractive candidate for current collector used in anode-free systems.

Herein, we systematically investigated the feasibility of employing commercial Cu-Zn solid solutions foils with varying Zn contents as current collectors for AFLMBs. Specifically, Cu-Zn solid solutions foil with Zn mass fractions of 32 %, 35 %, and 38 % ($Cu_{68}Zn_{32}$, $Cu_{65}Zn_{35}$, and $Cu_{62}Zn_{38}$), representing typical brass compositions, were used and compared with commercial Cu foil. For the exploration of the Zn and Cu-Zn intermetallic phase coatings, Zn coatings were introduced onto Cu foil using magnetron sputtering. Further, the Cu@Zn was thermally treated at 350 °C to generate Cu-Zn intermetallic phases, enabling a direct comparison between solid-solution alloys and intermetallic phases. Both Cu-Zn solid solutions foils and commercial Cu foil remain inert toward lithium alloying reaction during cycling, and the Cu-Zn solid solution with the highest Zn content ($Cu_{62}Zn_{38}$) exhibits favorable lithiophilicity and Li^+ diffusion kinetics, attributed to the uniform distribution of lithiophilic Zn within the Cu matrix. Although Zn and Cu-Zn intermetallic phase coatings display stronger lithiophilicity, they undergo lithiation/de-lithiation during cycling, leading to interfacial instability. This work highlights the unique advantages of Cu-Zn solid solutions, which simultaneously achieves chemical stability, lithiophilicity, and practical processability, offering a compelling alternative for current collector in AFLMBs.

To systematically evaluate the lithiophilicity and interfacial stability of Cu and various Cu-Zn based current collectors, first-principles calculations and electrochemical analyses were performed (Fig. 1). Fig. 1a shows the calculated formation energies and corresponding volume expansion ratios between a single lithium and different substrates. Cu and Cu-Zn solid solutions all demonstrate positive formation energies and minimal volume expansion, indicating their unfavorable lithiation tendency and excellent structural stability. In contrast, Cu-Zn intermetallic phases and pure Zn show negative formation energies, indicating a strong lithiation tendency. This enhanced reactivity leads to much higher volume expansion, which induces interfacial instability and non-uniform lithium deposition.

The lithium adsorption energies on various current collectors, a key indicator of surface lithiophilicity, are shown in Fig. 1b. Compared to Cu, Cu-Zn solid solutions exhibit enhanced lithiophilicity, which increases progressively with higher Zn content. Cu-Zn intermetallic compounds and pure Zn both exhibit enhanced lithium adsorption, with pure Zn displaying the highest lithiophilicity among all samples. These trends are consistent with electrochemical results of nucleation overpotentials (Fig. 1c and Figs. S1–S3 in Supporting information). All Cu-Zn solid solutions samples demonstrate much lower overpotentials compared to Cu, and the $Cu_{62}Zn_{38}$ with the highest Zn content exhibits the lowest nucleation overpotential, indicating its superior nucleation kinetics. In addition, the initial discharge curves of Cu-Zn solid solutions foils display no lithiation plateaus, confirming the absence of alloying reactions during cycling. In contrast, although Cu@Zn-350 °C and Cu@Zn electrodes exhibit stronger lithiophilicity, lithiation happens during the initial discharge process, consistent with their negative formation energies. This alloying reaction not only compromises interfacial stability but also consumes active lithium, thereby undermining the viability of anode-free configurations. Cyclic voltammetry (CV) test further validates these results (Figs. 1d and e). The peak intensities of $Cu_{62}Zn_{38}$, Cu@Zn-350 °C, and Cu@Zn electrodes are significantly higher than those of Cu, indicating their enhanced Li^+ transport kinetics. Notably, Cu and $Cu_{62}Zn_{38}$ electrodes exhibit no additional redox peaks, while Cu@Zn and Cu@Zn-350 °C electrodes show distinct initial reduction peaks, indicating alloying reaction happens. The half-cell cycling performances (Figs. S4–S6 in Supporting information) further corroborate these observations. As seen, $Cu_{62}Zn_{38}$ delivers the highest average Coulombic efficiencies (CE) of 98.7 % and superior long-term stability. The average CE of Cu@Zn and Cu@Zn-350 °C is 98.39 % and 98.5 %, respectively, primarily due to interfacial degradation from alloying. Cu foil fails after ~250 cycles due to its poor lithiophilicity and severe dendritic growth.

To gain further insights into the superior performance of Cu-Zn solid solutions, differential charge density analysis was performed on Cu and $Cu_{62}Zn_{38}$ adsorbed with single lithium (Fig. 1f). $Cu_{62}Zn_{38}$ shows stronger charge transfer and higher electron density accumulation at the lithium adsorption site, indicating enhanced electron transportation that facilitates lithium reduction. Furthermore, surface work function calculations for the (111) plane of Cu and $Cu_{62}Zn_{38}$ (Figs. 1g and h) reveal that $Cu_{62}Zn_{38}$ has a lower work function, suggesting more efficient interfacial electron transfer.

Building upon the crystal structure and surface properties discussed in Fig. 1, the phase composition and morphology of the current collectors were further analyzed (Fig. 2). The schematic diagram of the crystal structure of $Cu_{62}Zn_{38}$ is shown in Fig. 2a. The exposed Zn atoms on the surface serve as lithiophilic sites, significantly enhancing uniform lithium nucleation and promoting fast lithium diffusion, thereby enabling uniform and reversible lithium deposition. The X-ray diffraction (XRD) patterns (Fig. 2b and Fig. S7 in Supporting information) confirm the phase compositions of Cu and various Cu-Zn based current collectors. Compared to Cu, the diffraction peaks of $Cu_{62}Zn_{38}$ slightly shift to lower angles, indicating lattice expansion due to the incorporation of Zn atoms into the Cu matrix, consistent with its solid-solution structure. Cu@Zn shows diffraction peaks corresponding to Zn, confirming the successful introduction of Zn onto the Cu foil. Upon annealing at 350 °C, diffraction peaks of Cu_1Zn_1 and Cu_5Zn_8 intermetallic phases are observed in Cu@Zn-350 °C, suggesting that alloying reaction between Cu and Zn occurred under the heat treatment condition. Figs. 2c-e show the X-ray photoelectron spectroscopy (XPS) spectra for Cu and $Cu_{62}Zn_{38}$ foils, confirming the presence of Cu and Zn on the $Cu_{62}Zn_{38}$ foil surface. To investigate the surface morphology, scanning electron microscope (SEM) images of various current collectors are shown in Figs. 2f and g, Figs. S8 and S9 (Supporting information). Both Cu and $Cu_{62}Zn_{38}$ foils display a two-dimensional and planar morphology. Uniformly distributed Zn nanoparticles (~30 nm) are observed on the surface of Cu@Zn. Following heat treatment at 350 °C for 2 h, the Cu@Zn-350 °C sample exhibits morphological irregularities and partial aggregation, likely resulting from alloy formation processes. Fig. 2h presents the SEM-EDS mapping results of $Cu_{62}Zn_{38}$ foil, clearly demonstrating the uniform distribution of Cu and Zn elements.

To evaluate the lithium deposition behaviors of Cu and $Cu_{62}Zn_{38}$ current collectors, symmetric cells were assembled with pre-deposited lithium (2 mAh/cm^2). As shown in Fig. 3a, Cu exhibits higher polarization and significantly poorer cycling stability compared to $Cu_{62}Zn_{38}$. The $Cu_{62}Zn_{38}$ symmetric cell demonstrates lower overpotential and stable operation for over 1000 h. This su-

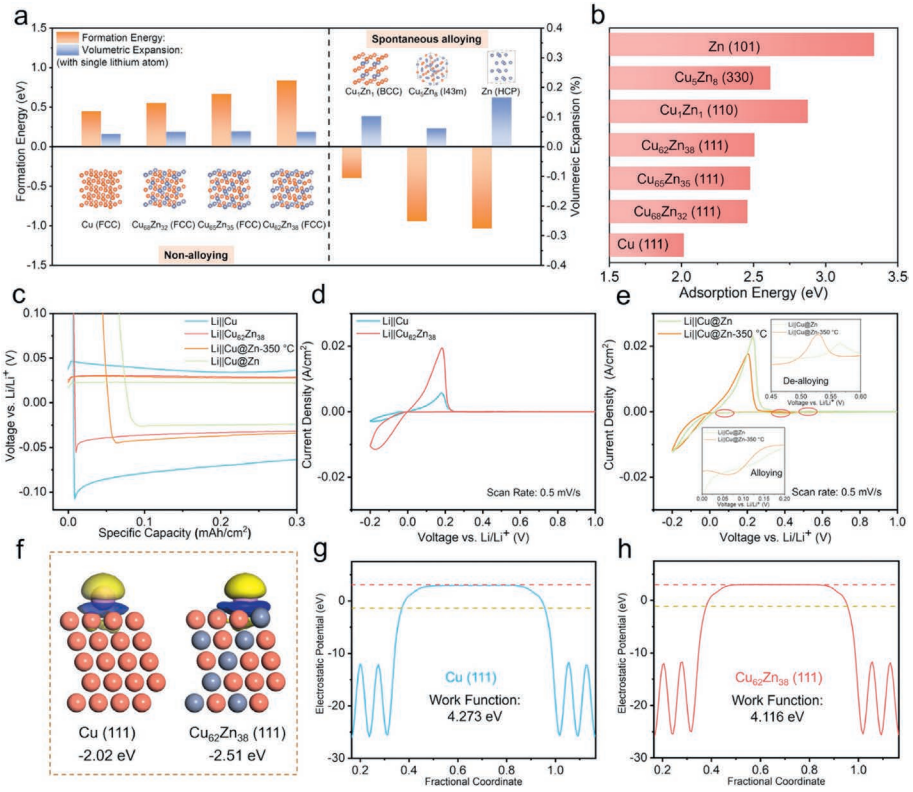


Fig. 1. (a) Formation energies and volume expansion ratios of single lithium with different substrates. (b) Li adsorption energies of different substrates. (c) The enlarged images of initial discharge curves of Li||Cu, Li||$Cu_{62}Zn_{38}$, Li||Cu@Zn and Li||Cu@Zn-350 °C half cells. (d) Cyclic voltammetry curves of Li||Cu and Li||$Cu_{62}Zn_{38}$ half cells. (e) Cyclic voltammetry curves of Li||Cu@Zn and Li||Cu@Zn-350 °C half cells. (f) Differential charge density of lithium adsorbed on Cu (111) and $Cu_{62}Zn_{38}$ (111) planes and (g, h) surface work functions of Cu (111) and $Cu_{62}Zn_{38}$ (111) planes.

perior electrochemical behavior of $Cu_{62}Zn_{38}$ was further confirmed by CV and electrochemical impedance spectroscopy (EIS) test (Figs. S10–S12 in Supporting information). As seen, $Cu_{62}Zn_{38}$ demonstrates significantly stronger oxide-redox signals and a higher exchange current density than Cu, indicating its enhanced electrochemical reactivity. EIS results also show lower impedance for $Cu_{62}Zn_{38}$, confirming its superior charge transfer capacity.

Further, Li||Cu and Li||$Cu_{62}Zn_{38}$ half-cells were assembled to evaluate the reversibility of lithium deposition. As shown in Figs. 3b-d, $Cu_{62}Zn_{38}$ demonstrates superior cycling performance and higher CE compared to Cu at various current densities of 0.5, 1, and 2 mA/cm^2, respectively. The corresponding nucleation overpotential results (Fig. 3e) reveal $Cu_{62}Zn_{38}$ has lower nucleation barriers, consistent with its superior electrochemical activity and stability. To precisely assess the average CE of the current collectors, the Aurbach test was employed (Figs. 3f and g). As seen, $Cu_{62}Zn_{38}$ exhibits higher average CE and lower polarization compared to Cu, highlighting its superior electrochemical performance.

To further investigate the electrochemical reactivity and Li^+ diffusion behaviors of the current collectors, CV, EIS and galvanostatic intermittent titration technique (GITT) tests were conducted. As shown in Fig. 3h, $Cu_{62}Zn_{38}$ shows much higher exchange current density (1.9×10^{-3} A/cm^2), indicating its enhanced electrochemical activity compared to Cu (3.18×10^{-4} A/cm^2). EIS measurements (Fig. S13 in Supporting information) reveal a lower charge transfer resistance for $Cu_{62}Zn_{38}$, suggesting improved ion transport and faster reaction kinetics. Moreover, the GITT results (Fig. S14 in Supporting information) indicate that $Cu_{62}Zn_{38}$ shows higher Li^+ diffusion coefficient (5.624×10^{-13}) than Cu (3.715×10^{-13}). These findings collectively highlight the enhanced electrochemical reactivity and ion diffusion capabilities of $Cu_{62}Zn_{38}$, which facilitates more uniform Li deposition.

Furthermore, *ex-situ* SEM characterizations were conducted on current collectors after depositing different amounts of lithium (Fig. 4a). At low deposition amounts, the $Cu_{62}Zn_{38}$ foil forms smaller and denser lithium nuclei, while the Cu exhibits irregular and coarse lithium depositions. This suggests that the excellent lithiophilicity of the $Cu_{62}Zn_{38}$ surface provides more uniform and dense nucleation sites. As the deposition amount increases, lithium metal is uniformly deposited on the $Cu_{62}Zn_{38}$ foil surface with a two-dimensional pattern, whereas the depositions are uneven and aggregated on the Cu foil, confirming the superior nucleation and growth behaviors of lithium metal on the $Cu_{62}Zn_{38}$ foil. These results further support the superior Li^+ diffusion capability of $Cu_{62}Zn_{38}$. DFT calculations reveal that $Cu_{62}Zn_{38}$ possesses a lower Li^+ diffusion barrier than Cu, suggesting enhanced ion transport kinetics (Fig. S15 in Supporting information). Additionally, finite element simulations based on the phase-field model were performed to study the lithium deposition behaviors on different current collectors using COMSOL Multiphysics 6.2 (Fig. 4a). $Cu_{62}Zn_{38}$ enables a more homogeneous and uniform lithium deposition. In contrast, Cu exhibits highly uneven deposition and favors dendritic Li growth. These simulation results are consistent with the SEM observations, further highlighting the critical role of surface lithiophilicity and Li^+ transport kinetics in dictating lithium depositing behaviors. Further, XPS depth profiling was employed to compare the SEI composition on the cycled Cu and $Cu_{62}Zn_{38}$ electrodes (Fig. 4b). The inner SEI on the $Cu_{62}Zn_{38}$ electrode is distinctly enriched in LiF (F 1s at 684.8 eV) and Li_3N (N 1s at 398.3 eV) compared to that on pure Cu, which are key components to its superior mechanical and ionic transport properties, explaining the excellent interfacial stability of the Cu-Zn solid solution current collector.

Anode-free batteries were assembled to evaluate the practical application of $Cu_{62}Zn_{38}$. As shown in Fig. 5a, $Cu_{62}Zn_{38}$ foil dis-

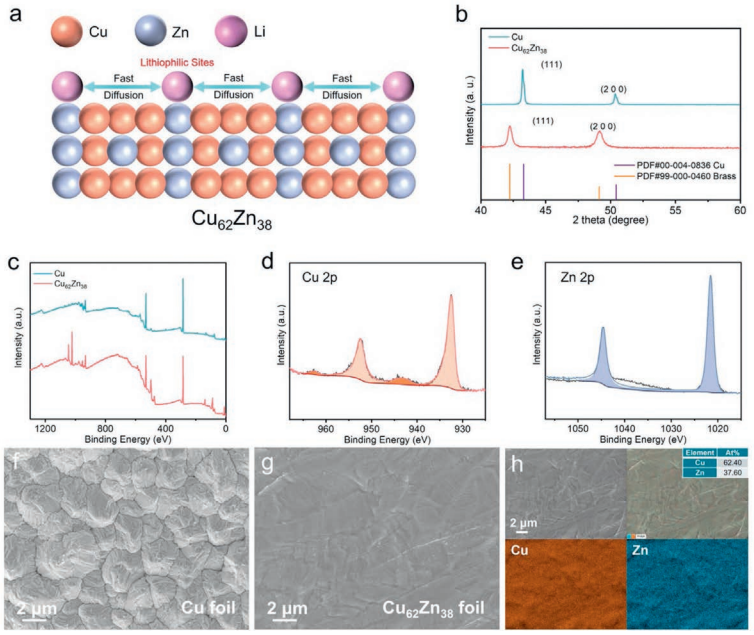


Fig. 2. (a) Crystal structure of Cu-Zn solid solution ($Cu_{62}Zn_{38}$), highlighting its structural advantages. (b) XRD patterns of Cu and $Cu_{62}Zn_{38}$. (c) XPS survey spectra of Cu and $Cu_{62}Zn_{38}$. (d) Cu 2p spectrum of $Cu_{62}Zn_{38}$. (e) Zn 2p spectrum of $Cu_{62}Zn_{38}$. (f, g) SEM images of Cu foil and $Cu_{62}Zn_{38}$ foil and (h) corresponding EDS mapping results of $Cu_{62}Zn_{38}$ foil.

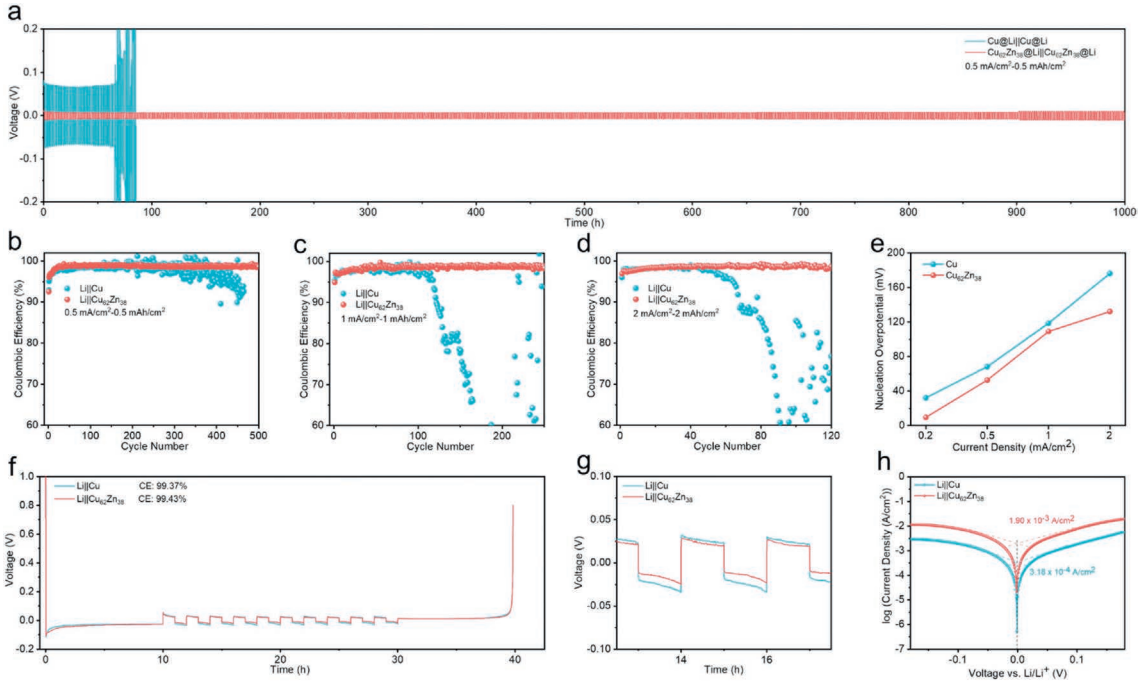


Fig. 3. Electrochemical performance of Cu and $Cu_{62}Zn_{38}$ in symmetric cells and half cells: (a) Cycling performances of Cu@Li||Cu@Li and $Cu_{62}Zn_{38}$@Li||$Cu_{62}Zn_{38}$@Li symmetric cells. (b–d) Coulombic efficiencies of Li||Cu and Li||$Cu_{62}Zn_{38}$ at 0.5 mA/cm^2–0.5 mAh/cm^2, 1 mA/cm^2–1 mAh/cm^2 and 2 mA/cm^2–2 mAh/cm^2. (e) Nucleation overpotentials of Cu and $Cu_{62}Zn_{38}$ at different current densities. (f, g) Aurbach test results of Cu and $Cu_{62}Zn_{38}$ and (h) exchange current density results of Li||Cu and Li||$Cu_{62}Zn_{38}$ half cells.

plays much superior cycling stability with a capacity retention of 55.1 % after 150 cycles under a 0.3 C/0.5 C charge/discharge protocol, while that of Cu is only 13.8 %. In addition, both Cu@Zn and Cu@Zn-350 °C demonstrates improved electrochemical performance than Cu, attributed to their superior lithiophilicity (Fig. S16 in Supporting information). However, their long-term cycling stability is invariably compromised. The repetitive volume changes of these coatings during lithiation/delithiation induce continuous mechanical degradation and interfacial reconstruction, leading to rapid capacity fade. In contrast, the $Cu_{62}Zn_{38}$ foil effectively avoids this issue due to its inherent structural stability. Fig. 5b also shows much better rate capability of $Cu_{62}Zn_{38}$ with a high capacity of 104.09 mAh/g even at a current density of 3 C. The initial charge-discharge curves (Fig. 5c) demonstrate an extremely weak nucleation overpotential for $Cu_{62}Zn_{38}$, confirming its excellent lithiophilicity. The higher reversibility of lithium deposition behaviors on $Cu_{62}Zn_{38}$ is also revealed by its higher initial Coulombic efficiency (86.92 %) than Cu (76.5 %). Furthermore, comparative charge-

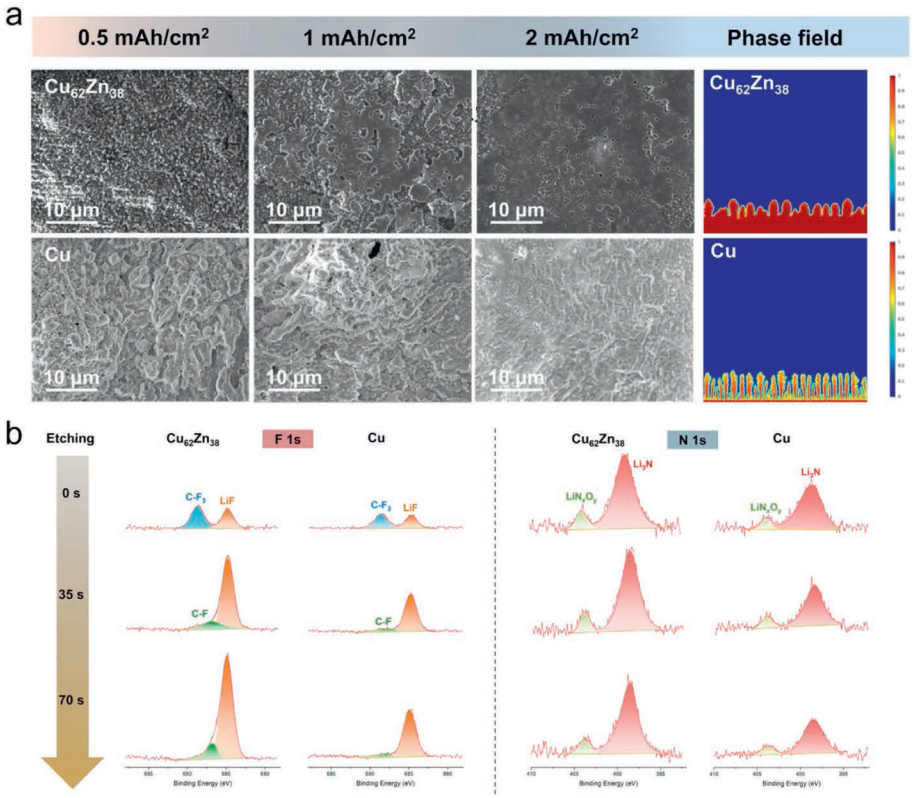


Fig. 4. (a) SEM images of Cu and $Cu_{62}Zn_{38}$ foils with different lithium deposition amounts and phase-field simulation results of lithium deposition on Cu and $Cu_{62}Zn_{38}$. (b) XPS spectra for F 1s and N 1s of the electrode surfaces of cycled Li||$Cu_{62}Zn_{38}$ and Li||Cu batteries.

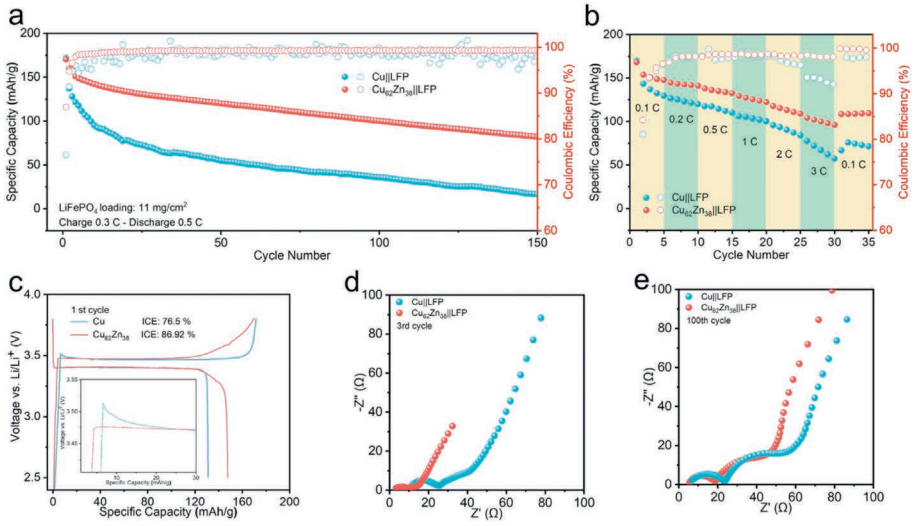


Fig. 5. (a) Cycling performance of Cu||LFP and $Cu_{62}Zn_{38}$||LFP anode-free batteries at 0.3 C charge and 0.5 C discharge rates with $LiFePO_4$ mass loading of 11 mg/cm^2, the batteries were first cycled for three cycles at 0.1 C. (b) Rate performance of Cu||LFP and $Cu_{62}Zn_{38}$||LFP anode-free batteries at increasing rates from 0.1 C to 3 C. (c) The charge-discharge curves of the first cycle of Cu||LFP and $Cu_{62}Zn_{38}$||LFP anode-free batteries and (d, e) EIS results of Cu||LFP and $Cu_{62}Zn_{38}$||LFP anode-free batteries after 3 cycles and 100 cycles, respectively.

discharge curves of Cu and $Cu_{62}Zn_{38}$ reveals superior stability in the Cu-Zn solid solution, evidenced by well-maintained voltage profiles across cycles (Fig. S17 in Supporting information). This enhanced cycling performance arises from $Cu_{62}Zn_{38}$'s improved lithiophilicity and robust interfacial stability. Supporting evidence from EIS measurements (Figs. 5d and e) demonstrates consistently lower SEI and charge transfer resistances than Cu, confirming stable interface formation and sustainable long-term cycling capability.

To further investigate the lithium deposition behaviors and structural stability of different current collectors during cycling, SEM images of the current collector surfaces at fully charged and discharged states after 100 cycles are shown in Figs. 6a-f. In the fully discharged state, both Cu and $Cu_{62}Zn_{38}$ exhibit noticeable particle residues, indicating the continuous accumulation of dead lithium during cycling. Upon further examination, the particles on the $Cu_{62}Zn_{38}$ surface are more uniformly distributed and smaller in size, whereas those on Cu are larger and dendritic morpholo-

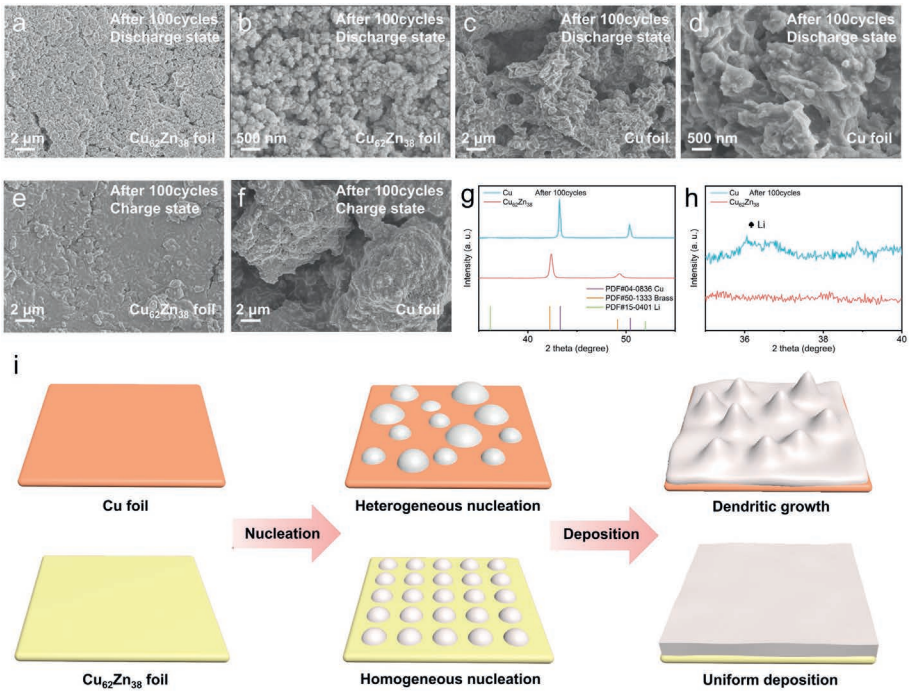


Fig. 6. SEM images of the current collector surfaces after 100 cycles: (a, b) $Cu_{62}Zn_{38}$ at fully discharged state, (c, d) Cu at fully discharged state, (e) $Cu_{62}Zn_{38}$ at fully charged state, and (f) Cu at fully charged state. (g, h) XRD patterns of Cu and $Cu_{62}Zn_{38}$ current collectors after 100 cycles and corresponding enlarged patterns and (i) the schematic illustration of lithium nucleation and deposition processes on different current collectors.

gies form. Results above suggest that the $Cu_{62}Zn_{38}$ current collector maintains a more stable interface and effectively suppresses dendrite growth during cycling. In the fully charged state, $Cu_{62}Zn_{38}$ current collector displays uniform two-dimensional depositing pattern, while Cu exhibits significant localized lithium aggregation. Furthermore, XRD analysis of Cu and $Cu_{62}Zn_{38}$ current collectors after 100 cycles (Figs. 6g and h) reveals distinct dead lithium signals in Cu, which are absent in $Cu_{62}Zn_{38}$. Based on the above discussions, a schematic diagram is presented in Fig. 6i to intuitively compare the distinct lithium nucleation and deposition behaviors on Cu and $Cu_{62}Zn_{38}$ current collectors. For conventional Cu foil, its intrinsically low lithiophilicity results in heterogeneous nucleation sites, which promotes the uncontrollable dendritic morphology form and leads to interfacial degradation during cycling. In contrast, $Cu_{62}Zn_{38}$ with a homogeneous distribution of lithiophilic Zn atoms provides energetically favorable sites for Li^+ adsorption and nucleation, enabling highly uniform lithium plating and maintaining a robust and stable interface throughout extended cycling. The combined structural integrity and superior lithiophilicity of $Cu_{62}Zn_{38}$ enable enhanced cycling performance, demonstrating its significant potential as a high-performance current collector for AFLMBs.

In summary, the Cu-Zn solid solution ($Cu_{62}Zn_{38}$) foil with superior lithiophilicity and fast Li^+ diffusion rate demonstrated significant potential for use in AFLMBs. The homogeneous Zn distribution within the solid solution significantly enhanced nucleation thermodynamics and stabilized growth dynamics. In contrast, although intermetallic coatings (Cu@Zn and Cu@Zn-350 °C) exhibited improved lithiophilicity, they experienced alloying reaction during cycling, leading to unstable interfaces and fast capacity degradation. Combined evidence from *ex-situ* SEM characterizations, COMSOL simulations and DFT calculations confirmed that $Cu_{62}Zn_{38}$ effectively suppressed dendrite growth and maintained electrochemical interface integrity through intrinsic alloying inertness. In anode-free batteries, the $Cu_{62}Zn_{38}$ foil demonstrated much superior cycling stability with a capacity retention of 55.1 % after 150 cycles, a fourfold improvement over conventional Cu foil (13.8 %). This work establishes Cu-Zn solid solution foil as an industrially scalable solution that extends AFLMB lifetime and efficiency *via* optimized Li^+ transport and interfacial control. Future integration of modified Cu-Zn solid solution current collectors with high-capacity cathodes (*e.g.*, Li-rich cathode) may unlock >400 Wh/kg AFLMBs, positioning them as a viable platform for next-generation high-energy batteries.

CRediT authorship contribution statement

Fan Zhang: Writing – original draft, Software, Formal analysis, Data curation. **Zizhu Guo:** Writing – original draft, Formal analysis, Data curation. **Jin Wang:** Software, Investigation, Data curation. **Dan Sun:** Supervision, Investigation, Formal analysis. **Xiaobing Huang:** Supervision, Resources, Project administration, Investigation. **Qi Zhang:** Supervision, Investigation, Formal analysis. **Yougen Tang:** Supervision, Project administration, Investigation. **Yusi Yang:** Supervision, Software, Resources, Formal analysis. **Haiyan Wang:** Writing – review & editing, Supervision, Project administration, Investigation, Funding acquisition.

Declaration of competing interest

The authors declare that they have no known competing financial interests or personal relationships that could have appeared to influence the work reported in this paper.

Acknowledgments

This research was financially supported by the National Natural Science Foundation of China (No. 22279164), the Hunan Provincial Science and Technology Plan Projects of China (No. 2017TP1001) and the Natural Science Foundation of Hunan Province (No. 2025JJ70677).

Supplementary materials

Supplementary material associated with this article can be found, in the online version, at doi:10.1016/j.cclet.2025.112057.

References

[1] S. Yang, Y. Wang, H. Pan, P. He, H. Zhou, Nature 636 (2024) 309–321.
[2] G. Harper, R. Sommerville, E. Kendrick, et al., Nature 575 (2019) 75–86.
[3] J. Xiao, F. Shi, T. Glossmann, C. Burnett, Z. Liu, Nat. Energy 8 (2023) 329–339.
[4] F. Schomburg, B. Heidrich, S. Wennemar, et al., Energ. Environ. Sci. 17 (2024) 2686–2733.
[5] J. Zhang, W. Xu, J. Xiao, X. Cao, J. Liu, Chem. Rev. 120 (2020) 13312–13348.
[6] H. Wan, J. Xu, C. Wang, Nat. Rev. Chem. 8 (2024) 30–44.
[7] S. Huo, L. Wang, B. Su, et al., Adv. Mater. 36 (2024) 2411757.
[8] Y. An, Y. Zeng, D. Luan, X.W.D. Lou, Matter 7 (2024) 1466–1502.
[9] L. Dong, S. Zhong, B. Yuan, et al., Angew. Chem. Int. Ed. 62 (2023) e202301073.
[10] S. Nanda, A. Gupta, A. Manthiram, Adv. Energy Mater. 11 (2021) 2000804.
[11] Y. Zhou, P. Wang, K. Wang, et al., Adv. Funct. Mater. 35 (2025) 2424022.
[12] J. Shi, C. Xu, J. Lai, et al., Angew. Chem. Int. Ed. 62 (2023) e202218151.
[13] M. Mao, X. Ji, Q. Wang, et al., Nat. Commun. 14 (2023) 1082.
[14] H. Su, H. Zhang, Z. Chen, et al., Chin. Chem. Lett. 34 (2023) 108640.
[15] K. Peng, X. Wang, X. Yan, Chin. Chem. Lett. 35 (2024) 109274.
[16] J. Sun, S. Zhang, J. Li, B. Xie, J. Ma, S. Dong, G. Cui, Adv. Mater. 35 (2023) 2209404.
[17] Q. Zhao, S. Stalin, L.A. Archer, Joule 5 (2021) 1119–1142.
[18] S. Zhang, H. Liao, Z. Liu, C. Yan, J. Huang, Chin. Chem. Lett. 35 (2024) 109284.
[19] X.L. Zhang, L. Ma, Y.P. Cai, J. Fransaer, Q. Zheng, Matter 7 (2024) 583–602.
[20] Z. Ouyang, S. Wang, Y. Wang, et al., Adv. Mater. 36 (2024) 2407648.
[21] C.Y. Im, G.Y. Lee, J.G. Kim, J.H. Choi, S.J. Kim, Adv. Mater. 37 (2025) 2501261.
[22] Z. Ouyang, Y. Wang, S. Wang, et al., Adv. Mater. 36 (2024) 2401114.
[23] J. Wang, Y. Wang, X. Lu, et al., Adv. Mater. 36 (2024) 2308257.
[24] H. Kwon, J.H. Lee, Y. Roh, et al., Nat. Commun. 12 (2021) 5537.
[25] Y. Wang, Y. Li, X. Wang, et al., Adv. Mater. 37 (2025) 2420373.
[26] S. Huang, S. Lu, Y. Lv, et al., Nano Res. 16 (2023) 11473–11485.
[27] S.K. Merso, T.M. Tekaligne, M.A. Weret, et al., Chem. Eng. J. 486 (2024) 149547.
[28] T.A. Nigatu, H.K. Bezabh, S.K. Jiang, et al., Electrochim. Acta 443 (2023) 141883.